Supporting information:

Nanoscale back contact perovskite solar cell design for improved tandem efficiency

Gede W.P. Adhyaksa, Eric Johlin and Erik C. Garnett*

Center for Nanophotonics, AMOLF, Science Park 104, 1098 XG Amsterdam, The Netherlands

* e.garnett@amolf.nl

1. Optical modelling

1.1. Acquiring optical constants

We acquired complex optical constants (*n-k*) of the materials from a combination of spectroscopic ellipsometry (SE) measurements and literature values. All *n-k* values used in our simulation are plotted in **Figure S1**. For the TiO_2, NiO_x, Al_2O_3, and fused SiO_2, the *n-k* values are based on SE measurements, whereas the *n-k* values for the FTO, $CH_3NH_3PbI_3$, and Si are taken from the literature. The TiO_2 and Al_2O_3 films were grown using atomic layer deposition (ALD) at 250^0C, while NiO_x film was deposited by a plasma-enhanced ALD. The films were further thermally annealed up to 480^0C (for TiO_2 and Al_2O_3), and 300^0C (for NiO_x) in ambient air for 60 min. This post annealing treatment enhances the metal oxide crystallinity which is important to get a high efficiency device. For example, the TiO_2 was converted from a resistive semi-amorphous phase to anatase crystalline films, with enhanced *n* values from ~1.7 to ~2.2 after the post-annealing. Using ALD, we could get a conformal, compact, and smooth films compared to the typical solution based process (e.g. sol-gel, chemical bath deposition, spray coating) which minimizes surface roughness, simplifying our SE model.

We used the *n-k* values for $CH_3NH_3PbI_3$ reported by Löper *et al*[1], which have an extremely sharp onset and small Urbach energy[2] (comparable to GaAs), and thus exclude any traces from an indirect bandgap contribution of $CH_3NH_3PbI_3$. For c-Si, FTO (Pelkington TEC 15), a-Si:H (i), and SiN_x the *n-k* values were taken from reported data by M.A.Green[3], Ball *et al.*[4], Pierce *et al.*[5], and Baker-Finch[6] respectively. For the metals in the nanogrid (Au), and rear-contact (Ag), we used the *n-k* values from Palik[7], and Johnson & Christy[8], respectively. The optical constant for n^{++}Si (front floating emitter, and rear-emitter), and p^{++}Si (back surface field) are set to be identical with standard c-Si. However, their free carrier absorption

effects are fully taken into account in our electrical simulations, as well as our optical path length calculations (details discussed below).

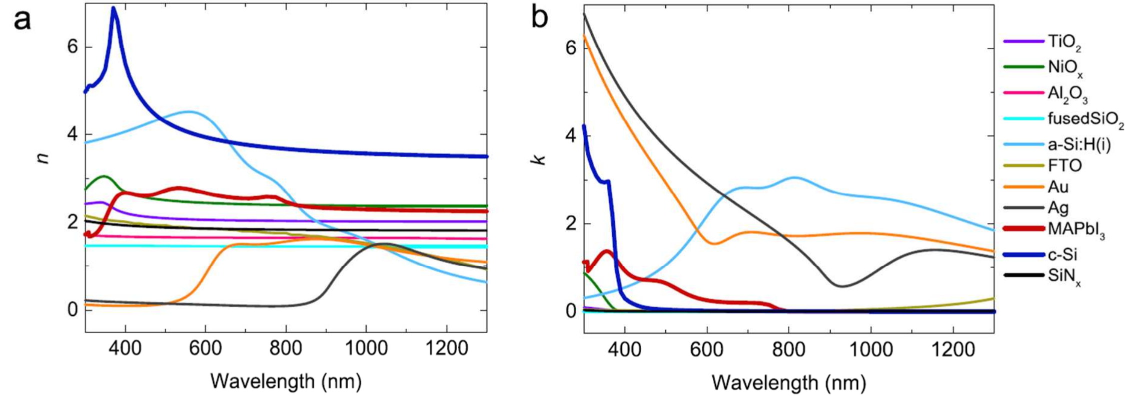

Figure S1. Refractive index of all materials used for the simulations: (a) the real part (*n*), and **(b)** the imaginary part (*k*). The *n-k* for a-Si:H(i), FTO, Au, Ag, $MAPbI_3$, c-Si, and SiN_x are reported values from the literatures[3-8], while values for TiO_2, NiO_x, Al_2O_3, and fused-SiO_2 are obtained from ellipsometry measurements.

1.2. Optical simulation setup

1.2.a. Interface and data processing:

The optical simulations were performed in two different modules using (1) full-field electromagnetic wave calculations based on a finite different time domain method (FDTD, Lumerical, Inc.)[9] for the perovskite cell, and (2) a rigorous polarization ray tracing solver (OPAL2, PV Lighthouse Pty. Ltd.)[10] for the Si cell. The two different methods are implemented due to the thickness difference between the two cells (< 1 μm for perovskite vs. 180 μm for Si). As a consequence, light propagations in both cells are computed differently (coherent vs. non-coherent for perovskite vs. Si cells, respectively). The two methods are coupled by using output from the FDTD (optical transmission modes weighted over AM 1.5 spectrum) as an input/filter for the ray tracing solver.

To get an accurate result of all optical interferences between the top and bottom cell interfaces, we extend the simulation ~1 μm down to the Si for the 2-T and 3-T (IBC) tandems. This is important, because the perovskite and silicon cells in both cases are optically coupled. However, for the 4-T tandem, the two cells are optically decoupled, but we still included an

interference contribution from the SiO_2 spacer (framed down to ~1 μm out of 10 μm from its actual thickness). A weighted transmission modes from this SiO_2 spacer (~10 % of the thickness) is used as the input for the ray tracing calculation in the 4-T tandem, and in this case SiO_2 spacer is used as a superstrate.

Besides the original packages provided by the FDTD and ray tracer modules, we carried out our computational routines using Python codes to couple results from those two packages. The routine includes calculations of charge generation rate inside cavities, effective collection distance, optical path length enhancement, total reflectance, and sweeping PV parameters.

1.2.b. Perovskite solar cells:

One unit cell is defined as a square with side lengths of the nanowire grid spacing, centred at the grid intersection. We use anti-symmetric boundary conditions for the x-axis, symmetric boundary conditions for y-axis, and perfectly matched layers (PMLs) for z-axis, allowing us to simulate a quarter of the unit cell area. A broadband plane wave (λ = 300 – 1300 nm; 1 nm interval) at normal incident (propagating toward the structure along the z-axis) is launched from the top of the structure as incident source, with polarization either from x- or y-axis. The simulation employs a cubic mesh with a mesh size of 5 nm, and to obtain a sub-accuracy, a 1 nm refinement is employed along the grid-perovskite and TiO_2 perovskite interfaces. Prior to running the simulation, all of the optical constants are imported into the material database, and modelled by multi-coefficient fitting (λ = 300 – 1300 nm) until reaching a global minimum RMS error. For the perovskite, the multi-coefficient fitting provided by the FDTD gives a slightly larger error after 900 nm wavelength which deviates the k-optical constant to be above zero which physically does not exist. So, we manually set the k values to be 0 above 900 nm.

A frequency profile monitor is used to detect the electric field across the structures. Transmission is monitored with power monitor placed below the structure (TiO_2/a-Si:H(i) interfaces for 3-T, NiO_x/a-Si:H(i) interfaces for 2-T, and rear-FTO (perovskite)/glass (spacer) interface for 4-T); see schematic tandem structure (**Fig. S2**). Absorption is computed by calculating a ratio of power absorption from each electric field vector component integrated over the volume of the material. An optical charge generation rate (G) can be computed spatially over the $CH_3NH_3PbI_3$ structures by multiplying the electric field intensity ($|E|^2$), and imaginary part of permittivity (ε'') of the $CH_3NH_3PbI_3$ over twice angular frequency Plank constant ($2\hbar$)[22]; $G(\omega) = [\varepsilon''|E|^2]/2\hbar$. Reflection is monitored with power monitored placed on

top of the structure and behind the source. Note that, this is just a reflection mainly contributed by the perovskite cells structures only, and partially (but not fully) by the Si cells (since we also incorporated interference ~1 μm down to the Si cells). Reflections from the silicon back interface are incorporated in the following section.

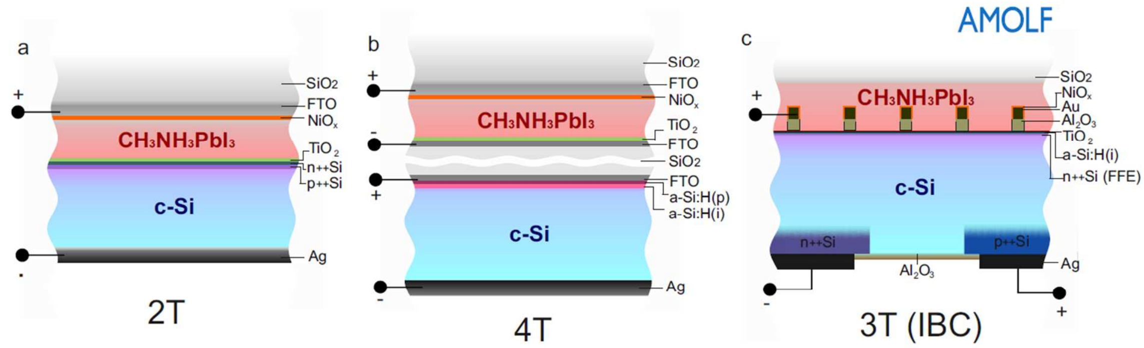

Figure S2. Schematic (cross-section view) of planar perovskite-silicon tandem architectures used in this work. (a) 2-T, (b) 4-T, and (c) 3-T (IBC). The schematics are drawn not to scale.

1.2.c. Silicon solar cells:

For the Si bottom cell, the source of illumination is computed by weighting the optical transmission through the top perovskite cell with AM 1.5 solar spectrum at normal incidence. In addition to this, for 4-T tandem, the fused SiO_2 spacer (10 μm), and FTO (Si top contact) are incorporated by calculating the transfer matrix from the perovskite to the FTO and Si cell. This FTO acts as an anti-reflective coating (**Fig. S3**) for the Si bottom cells in the 4-T, and later on explains why the EQE of Si cell is higher in the 4-T compared to the 2-T; given the fact that perovskite thickness used in the 4-T (950 nm thick) is thicker than the 2-T (300 nm thick) at their optimum efficiency. We calculated the reflection, transmission, and absorption of the (planar) Si cell by taking into account an optical path length enhancement (Z) dependent over the broadband range (λ = 300 – 1300 nm).

The optical path length enhancement inside the Si cell mainly occurs because of non-negligible specular reflection both from the rear Ag metal contact and scattering from the nanoscale metal grid contact within the perovskite (increasing the average angle of incident light on the silicon interface). These effects cause the optical path length to be greater than the actual Si cell thickness; where Z is defined as the ratio of the optical thickness and actual thickness ($Z = t_{opt}/t$). Using our computational routine, we solved the $Z(\lambda)$ analytically for

each tandem configuration by taking into account the reflectance (in both sides) based on the actual structures obtained from FDTD simulations. Free-carrier absorption losses from the front floating emitter (FFE), back-surface field (BSF), and rear-emitter (detail characteristics described in the electrical modelling part) were also incorporated into the $Z(\lambda)$ calculation.

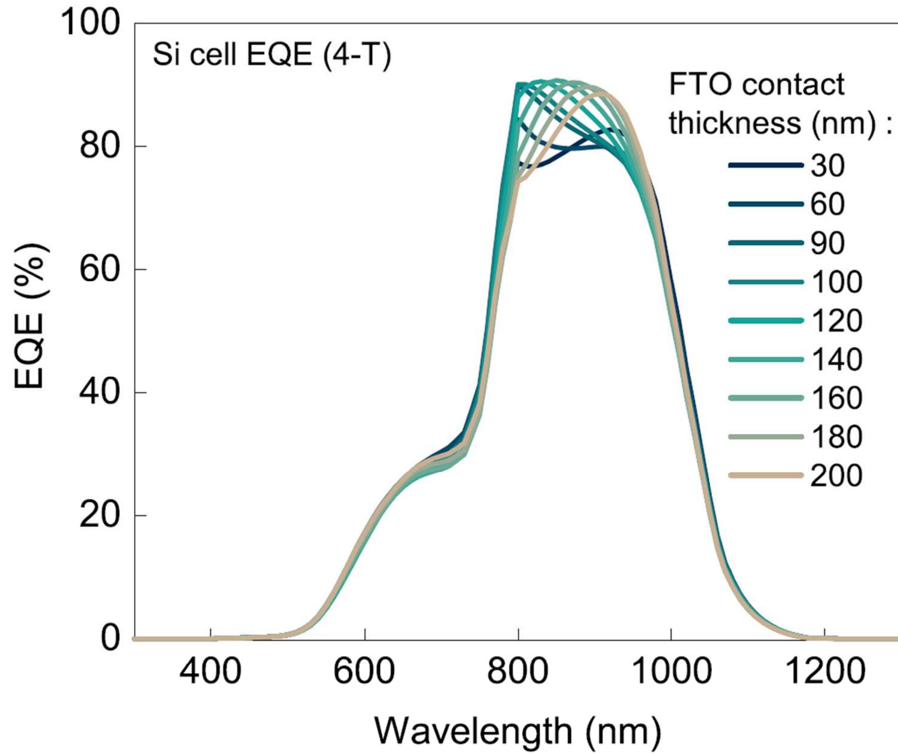

Figure S3. Silicon cell EQE in the 4-T with different FTO thickness. It shows the FTO contacts can act as anti-reflective coating on the Si cell in the 4-T.

The generation rate ($G(\lambda)$) for Si cell can be directly calculated as a Beer-Lambert decay of the optical transmission modes ($T(\lambda)$) multiplied by the absorption coefficient ($\alpha(\lambda)$) over the Si optical cell thickness: $G(\lambda) = \alpha(\lambda)T(\lambda)e^{-(\alpha(\lambda).z(\lambda).t)}$. The total generation rate (G) is calculated by accumulating the $G(\lambda)$ over the simulated wavelength range $\lambda = 300 - 1300$ nm.

For the limiting case (heretofore is essentially the actual optical limit taking into account all of the optical interferences), we used PV parameters calculated based on our optical simulation: (1) The optical short-circuit current (J_{opt}) is directly calculated by multiplying the total generation rate (G) with elementary charge constant (q) by assuming 100 % collection efficiency and infinitely long diffusion length; (2) The optical open circuit voltage (V_{opt}) is calculated based on the standard diode equation using ideality factor (n) of 1,

and 2 for perovskite, and silicon cells, respectively. For perovskite cell, there are some variants of the diode ideality factor reported in literatures depending on the materials quality and device architectures. In this optical simulation, the n=1 is used to emphasize that the main recombination is purely through radiative recombination; (3) The optical fill-factor (FF_{opt}) is determined according to a well-known empirical equation[11]. All PV parameters obtained in this optical simulations are tabulated and compared together with the coupled optical-electrical ones in **Figure S4**.

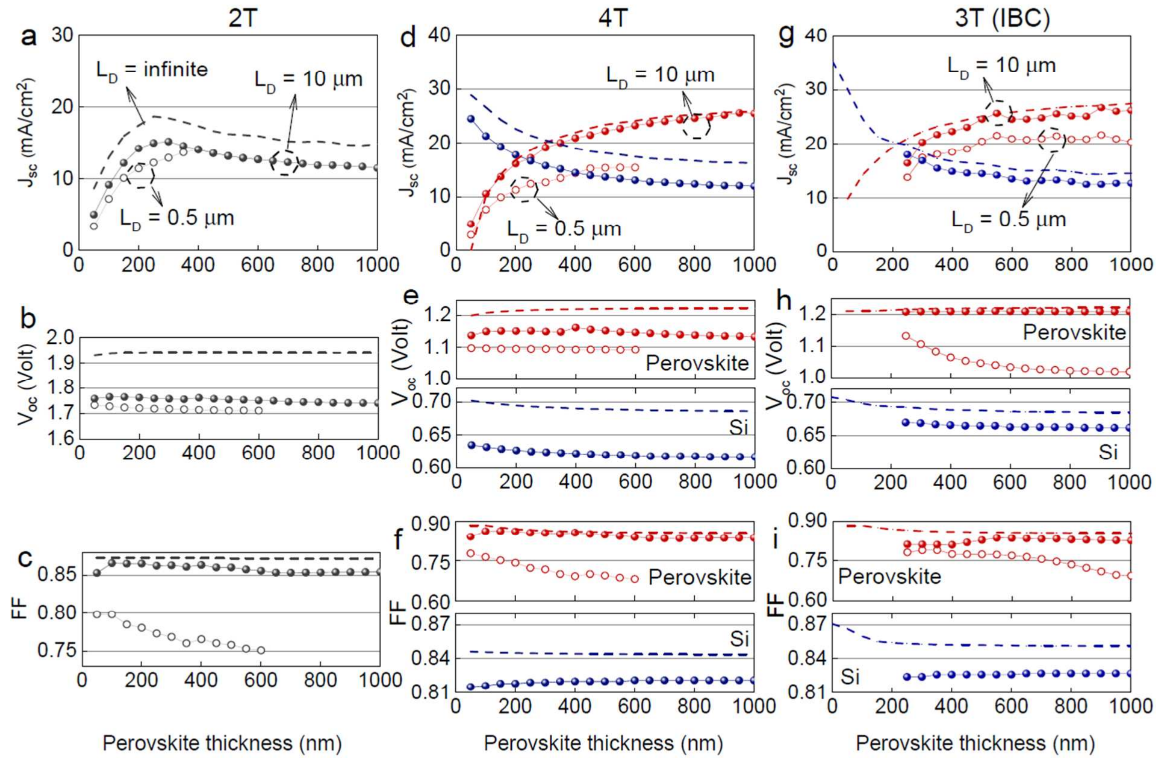

Figure S4. PV parameters of the perovskite-silicon tandem obtained from the optoelectronics simulations. The performance is examined using two different qualities of perovskite minority carrier diffusion lengths (indicated as L_D = 0.5 μm and 10 μm). For the 2-T configuration, the current-matching condition (series connection) is applied with 100 % tunnelling efficiency from top to bottom cells, and so only the tandem performances is plotted here (**Fig. S4a-c**). For the 4-T, the top-bottom cells are operated independently where contribution from perovskite (red lines) and silicon (blue lines) cells are shown (**Fig. S4d-f**). In the 4-T with the 0.5 μm diffusion length, perovskite cells with a thickness above 600 nm are not simulated due to limited charge collection. For 3-T (IBC) configuration, the two cells

are treated to be electrically decoupled with 100 % tunnelling efficiency from top to the bottom cell where the respective two cell performances are presented (**Fig. S4g-i**). In the 3-T (IBC), cells with perovskite thickness less than 250 nm were not simulated due to thickness restriction of the internal nanowire grid network. All of these optoelectronics PV parameters (solid lines) are compared with the PV parameters obtained purely from the optical simulations (curves with dashed lines); indicating the limiting performances. The tandem efficiencies for the 2-T, 4-T, and 3-T (IBC) are presented in figure 3 (main text).

1.2.d. Optical path length enhancement for planar Si cells:

The optical path length enhancement is defined as a ratio between the optical thickness and the actual thickness of the Si cells. The optical thickness becomes more than the actual Si thickness when the photon experiences multiple reflections from the front and rear surfaces of the Si cells. Although our tandem configurations are planar without any use of texturing/light trapping schemes, the enhancement is still significant, in particular for 3-T (IBC) tandem case where we have nanogrid network (containing Au metal), and metal rear contact (Ag back reflector) on top and bottom of the Si cells, respectively, thus resulting multiple internal reflections inside the Si cells. The influence of the nanowire mesh is incorporated through the calculations of the electric field immediately after propagation into the silicon layer, which are then transformed to the far-field, providing the angular distribution of the incident irradiation. From the angular distribution, an effective angle, φ, for the light entering the silicon layer is computed, and the path length is then adjusted by $Z(\lambda)_{scat} = 1/\cos(\varphi)$. We formulate the optical path length enhancement for each wavelength $Z(\lambda)$ as:

$$Z(\lambda) = Z(\lambda)_{scat} \cdot \sum_{i=1}^{\infty} \{ I_0(\lambda) + [I_{i-1}^{D}(\lambda) \cdot (R(\lambda)_{Ag} - L(\lambda)_{BSF} - L(\lambda)_{Emit})] + [I_{i-1}^{U}(\lambda) \cdot (R(\lambda)_{Grid} - L(\lambda)_{FFE})] \} \tag{S1}$$

where $Z(\lambda)_{scat}$ is effective path length enhancement due to scattering from the nanogrid networks towards Si cells, $I_0(\lambda)$ is incoming photon towards Si cells (or transmission from the top cells), $I_{i-1}^{D}(\lambda)$ is incoming photon facing *down* toward the rear of Si surfaces, $I_{i-1}^{U}(\lambda)$ is incoming photon facing *up* toward the front of Si surfaces, $R(\lambda)_{Ag}$ is the reflection from the silver surfaces toward Si, $R(\lambda)_{Grid}$ is the reflection from the grid toward Si, $L(\lambda)_{BSF}$ is losses from the back-surface field, $L(\lambda)_{Emit}$ is the losses from the rear-emitter, $L(\lambda)_{FFE}$ is losses from the front-floating emitter. These losses are due to free-carrier absorption from the highly

and heavily doped Si, and modelled using classical Drude's model absorption[12]. The iteration is repeated until either $I_{i-1}^{D}(\lambda)$ or $I_{i-1}^{U}(\lambda)$ is < 0.0001.

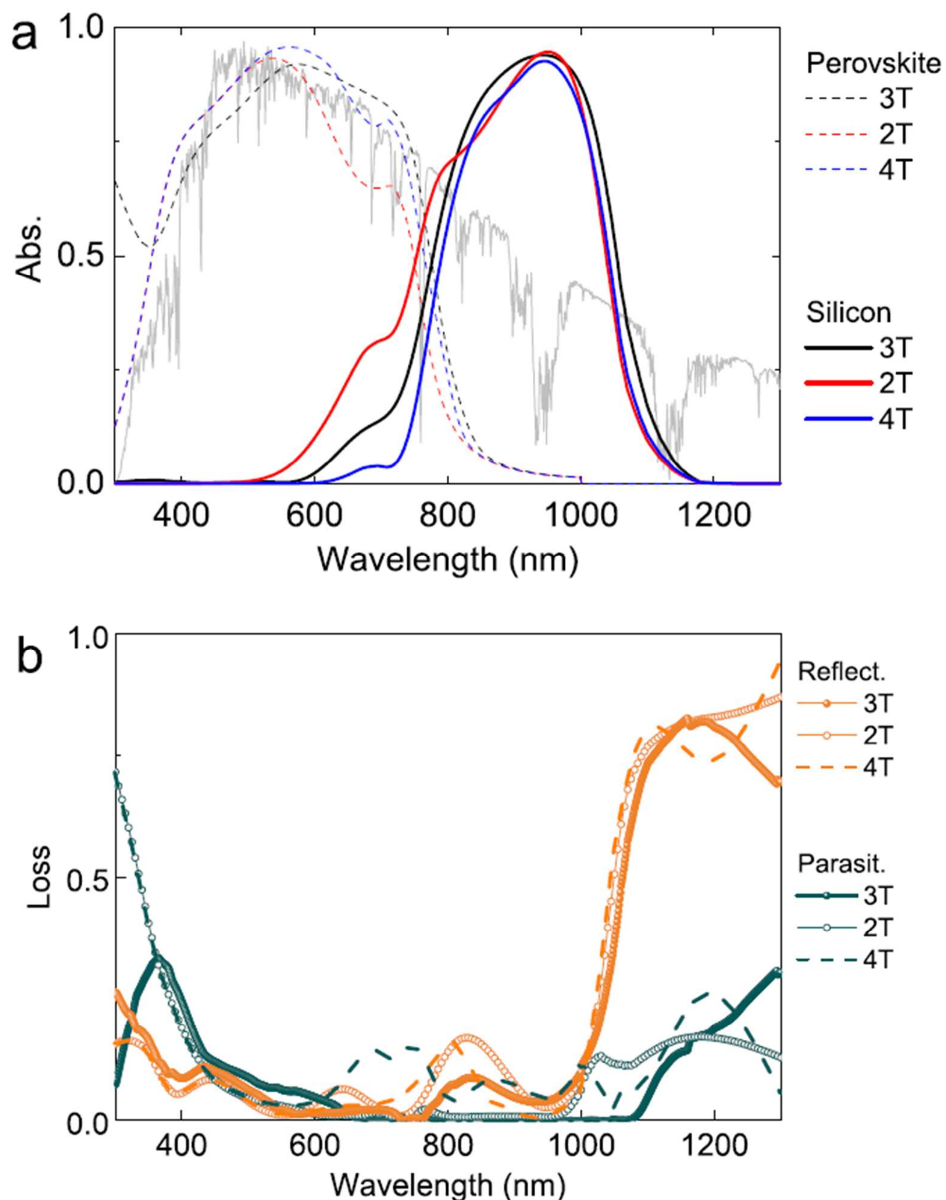

Figure S5. Spectra responses of the perovskite-silicon devices with 2-T, 4-T, and 3-T (IBC) tandem configurations. **(a)** Absorption (compared with AM 1.5 standard spectrum; grey line), and **(b)** Losses (reflection and parasitic absorption). These spectra responses were simulated at optimum conditions for each tandem configuration (at perovskite thickness of 300 nm, 950 nm, and 550 nm for 2-T, 4-T, and 3-T (IBC), respectively). Note that the parasitic absorption of both 2-T and 4-T tandem increases up to ~0.74 at 300 nm wavelength.

1.2.e. Total reflection losses for the 3-T (IBC) tandem:

Simulating total reflection (**Figure S5**) in the 3-T (IBC) is not as straight forward as in the 2-T and 4-T tandem configurations, because we need to take into account the effect of optical path length enhancement from the Si cell that intuitively should reduce the reflectance obtained from FDTD. However, we can formulate the upper bound of the total reflection $R_{tot}(\lambda)$ as:

$$R_{tot}(\lambda) = R_{Top}(\lambda) + R_{Bottom}(\lambda) \quad \text{(S2)}$$

$$= R_{Top}(\lambda) + T_1(\lambda)[1 - A_{Si}(\lambda)]T_2(\lambda) \quad \text{(S3)}$$

$$= R_{Top}(\lambda) + T_1(\lambda)\left[1 - \left(\left(1 - e^{-(\alpha(\lambda).Z(\lambda).t)}\right)T_1(\lambda)\right)\right]T_2(\lambda) \quad \text{(S4)}$$

where $R_{Top}(\lambda)$ is the reflection contributed by the perovskite top cell (with all gridline involved), $\alpha(\lambda)$ is the absorption coefficient of the Si, $Z(\lambda)$ is the optical path length enhancement (calculated from the equation S1), t is the Si thickness (180 μm), $T_1(\lambda)$ is transmission from the perovskite to the Si cell, and $T_2(\lambda)$ is transmission from the Si back into the perovskite. $R_{Bottom}(\lambda)$ is reflection contributed by the Si cell, calculated from the transmissions ($T_1(\lambda)$ and $T_2(\lambda)$) and attenuated by the losses from the Si cell absorption ($A_{Si}(\lambda)$). The total reflectance loss in the 3-T (IBC) is 12.4 mW/cm^2, which is less than the 2-T, and 4-T configurations (13.7 mW/cm^2 and 12.9 mW/cm^2 for 2-T and 4-T, respectively). The reflectance loss in the 4-T is quite similar to the 3-T (IBC), due to the optimized FTO layer, which serves as anti-reflective coating for the Si bottom cell (**Figure S3**).

2. Electrical modelling

2.1. Determining the electrical properties

All electrical parameters are listed in **Table S1**. These values were modelled based on values reported in literature. For the perovskite ($CH_3NH_3PbI_3$), we assume that the charge transport is equal for electrons and holes, although asymmetric transport is possible (e.g. by chloride addition into the iodide mixture; $CH_3NH_3PbI_{3-x}Cl_x$)[13]. We assume that the dominant recombination pathways are trap-assisted (Shockley-Read-Hall) and electron-hole radiative recombination, whereas Auger recombination process is assumed to be less competitive in our simulation (which is valid at the steady-state 1 sun illumination)[14]. The electron (TiO_2), hole (NiO_x) transporting layers, and the dielectric insulator (Al_2O_3) are modelled as semiconductors with doping profiles simulated using a selective junction model (Helmholtz

Zentrum, AFORS-HET)[15]. The profile basically depends on the density-of-states (DOS) of materials set in the simulation inputs.

For Si cells, parameters of electron/hole mobility, lifetime, dark current, sheet, and base resistance are modelled based on doping concentration (computed using calculators provided by PV lighthouse); doping profile is simulated using classical Drude model. Auger recombination is included in our calculations for both planar and textured Si cells. The effect becomes higher in the textured cells because of a higher excess carrier concentration. For example, on the front surface of Si the Auger recombination rate is ~10^{32} $cm^{-3}s^{-1}$ for the textured device, and ~10^{26} $cm^{-3}s^{-1}$ for the planar Si cell.

Table S1. Material properties used for the electrical simulation

Materials	Electrical properties										
	$E_g^{\perp}$ (eV)	$m^{*\#}$		ε_{DC}¶	χ†† (eV)	μ† (cm^2/V.s)		τ‡ (ns)		$R_S^{\|\|}$ (Ω/sq)	J_0 (mA/cm^2)
		e^-	h^+			e^-	h^+	e^-	h^+		
$CH_3NH_3PbI_3$	1.55	0.104	0.104	6.5	3.9	30	30	<10^4	<10^4	-	1.7×10^{-20}
TiO_2	3.2	-	-	9	3.92	0.2	0.1	5	1	-	-
NiO_x	3.25	-	-	11.9	1.46	0.1	0.2	1	5	-	-
Al_2O_3	6.7	-	-	9.34	4.02	0.1	0.1	1	1	-	-
Au grid	-	-	-	37	5.1	-	-	-	-	0.85-13	-
FTO	3.5	-	-	9.0	4.1	-	-	-	-	6	-
a-Si:H (i)	1.8	0.34	0.34	7.2	3.95	20	5	0.32	1.28	-	-
n^{++}Si (FFE)	1.09	1.18	0.809	11.7	4.62	150	150	6×10^4	6×10^4	70	6×10^{-11}
(p-type) c-Si	1.12	1.18	0.809	11.7	4.59	470	1471	3×10^6	4×10^6	1000	3×10^{-10}
n^{++}Si (emitter contact)	1.09	1.18	0.809	11.7	4.62	150	-	6×10^4	-	55	3×10^{-7}
p^{++}Si (BSF contact)	1.09	1.18	0.809	11.7	4.62	-	150	-	6×10^4	40	1.5×10^{-7}

⊥ Effective electronic bandgap at 300 K that is modelled using Varshni's coefficient. For Si, doping dependent is also modelled that accounts for narrowing the bandgap; **#** Effective mass which is used to calculate the density of states (DOS) at valence and conduction band using the Fermi-Dirac statistics; ¶ Relative dielectric constant (relative permittivity) at zero frequency (DC); †† Work-function (vs. vacuum level); † Charge mobility; ‡ Charge lifetime where the values are varied (with fixed mobility) to obtain different values of minority charge diffusion length (L_D); where $L_D = [(k_BT/q).\ \mu.\ \tau]^{1/2}$. For c-Si, the Auger recombination model was also taken into account; || Sheet resistance; we also incorporated a shunt resistance (R_{sh}) in the external circuit to be 10^5 Ω/cm^2. For the Au, the sheet resistance is calculated based on equivalent resistivity ranging across the different pitch sizes. For Si cell, to optimize the FFE performance, the base resistance of the c-Si should be higher than the n^{++}Si; **§** Dark-saturated current density where the ideality factor are 1 and 2 for perovskite and Si cells, respectively.

2.2. Electrical simulation setup

2.2.a. Interface and data processing:

The electrical simulation was performed by numerically solving the electrostatic potential and drift-diffusion transport equations under finite element based method using two different simulation modules (1) DEVICE CT (Lumerical, Inc[16].) for perovskite cells, and (2) Quokka2 (PV Lighthouse Pty. Ltd[17]) for Si cells. The treatments were due to the large different thickness in the two cells (< 1 μm for perovskite vs. 180 μm for Si). We used spatial charge carrier distributions (generated from the optical simulation above) as inputs for our electrical simulations. While complex behaviour of the CH_3NH_3 ions has been shown to create hysteresis in current-voltage response curves of perovskite materials, most high efficiency perovskites actually do not pose such behaviour,[18] and so this influence is neglected here. For the Si cells, we also consider optical path length enhancement in the charge generation rate calculation (see the *Si cells* discussion below). Note that both modules themselves currently are not able to model a tunnel junction, because the provided tunnel model is based on a quantum-mechanical process (band-to-band tunnelling models of Hurkx-Schenk)[19]. So, we computed analytically the electrical transmission from the top to the bottom cells by adopting Ebers-Moll model of bipolar transistor with a unity gain (the non-unity gain is also examined, see **Fig. S6**). We used identical geometrical tandem devices as described in the optical simulation. All simulations are conducted at a temperature of 300 K.

2.2.b. Perovskite solar cells:

We applied a tetrahedron 3D coarse mesh (with 20 nm length constraints), and auto mesh refinement across a change in doping density (typically ~10 times smaller than the geometrical sizes). A boundary condition controlling the bias is set on both Au metal nanowire grid (emitter) and n^{++}Si (base) where a steady-state DC sweep is run from -0.2 to 1.6 V applied voltage (0.02 V interval). We used Gummel's numerical method for a self-consistent control for the calculation, iterating between calculating the drift-diffusion equation and used it as an input to solve Poisson's (electrostatic potential) equation, *vice versa*. This iteration was carried out until absolute tolerance $< 10^{-6}$ V to reach the convergence. We used the output containing the spatial information of the electrostatic potential, the electron-hole distribution, recombination rates, and mobility in order to compute the perovskite PV characteristics (J, V, FF), and EQE (in this case using multistep single frequency generation rate rather than broadband plane wave input on the FDTD optical simulation). All PV

parameters for perovskite cells can be seen in the **Figure S4**; all of which are in a good agreement with experimental values of high efficiency perovskite solar cells.

2.2.c. Silicon solar cells:

For the silicon cells, we used 1D charge generation rate profiles as the inputs into the electrical simulations. These were calculated by first multiplying the optical transmission (from the perovskite cells after passing through all layers before reaching the c-Si interface, and weighted over the AM 1.5 spectrum) with absorption coefficient of the c-Si, and multiplied by the Beer-Lambert exponential decay of absorption coefficient with the distance over the Si thickness. For the 3-T (IBC) tandem, since the nanowire grids (on Perovskite) and metal back contact (on Si) can create internal reflection increasing the optical path, we compute the optical path length enhancement as a function of wavelength and then incorporated it into the generation rate matrix of Beer-Lambert calculation. Finally, the matrix of generation rate is integrated over 300 – 1300 nm wavelength across the distance of Si thickness.

An orthogonal conformal mesh is used for domain discretization to solve the drift-diffusion and electrostatic transport equation in 3-D simulations for 3-T (IBC) tandem, and 2-D simulations for 2-T and 4-T tandems (2-D simplification offers faster computational time, while yields only < 0.01 % deviation compared to the 3-D; likewise, it is not possible for the 3-T (IBC)). A conductive boundary approach is used in the simulation meaning that the diffusive transport at the space-charge regions (e.g. interface between c-Si and BSF, emitter, or FFE) is treated as recombination losses, while outside of these regions the transport is in quasi-neutral state. At the space-charge regions the surface recombination velocity, non-ideal dark saturation current densities, and contact resistivity are obtained using an analytical calculator provided by PV Lighthouse Pty. Ltd (EDNA2). According to a suggestion provided by Fell et.al[17], for self-consistency check, we run the simulation using different mesh refinement qualities (“coarse”, “medium”, “fine”), and relatively no mesh dependency is observed (less than 0.2 % variation). We calculate the PV parameters of the Si cells by running a DC-sweep from 0 to 0.7 V with 0.05 V interval. All PV parameters for Si cells obtained in this simulation are tabulated in **Figure S4**. The EQE of the Si cells is calculated using monochromatic (instead of broadband) generation calculations. This assumes 100 % injection efficiency, and even with a 15 % loss in the injection, the 3-T (IBC) tandem performance reduces by < 2 % absolute power conversion efficiency (**Figure S6**).

2.2.d. Tunnel junction for 3-T (IBC) tandem:

The tunnel junction is one of the critical components in our 3-T (IBC) tandem architectures. It is composed of interfaces from TiO_2/a-Si:H (i)/n^{++}Si front floating emitter (FFE). The FFE is saturated with electrons injected from perovskite to TiO_2/a-Si:H (i), and from n^{++}Si back surface field (BSF)/p-Si base. Additionally, the generated electron (minority carriers) from the p-Si base will first diffuse to n^{++}Si and then will be injected back to the p-Si base[20].

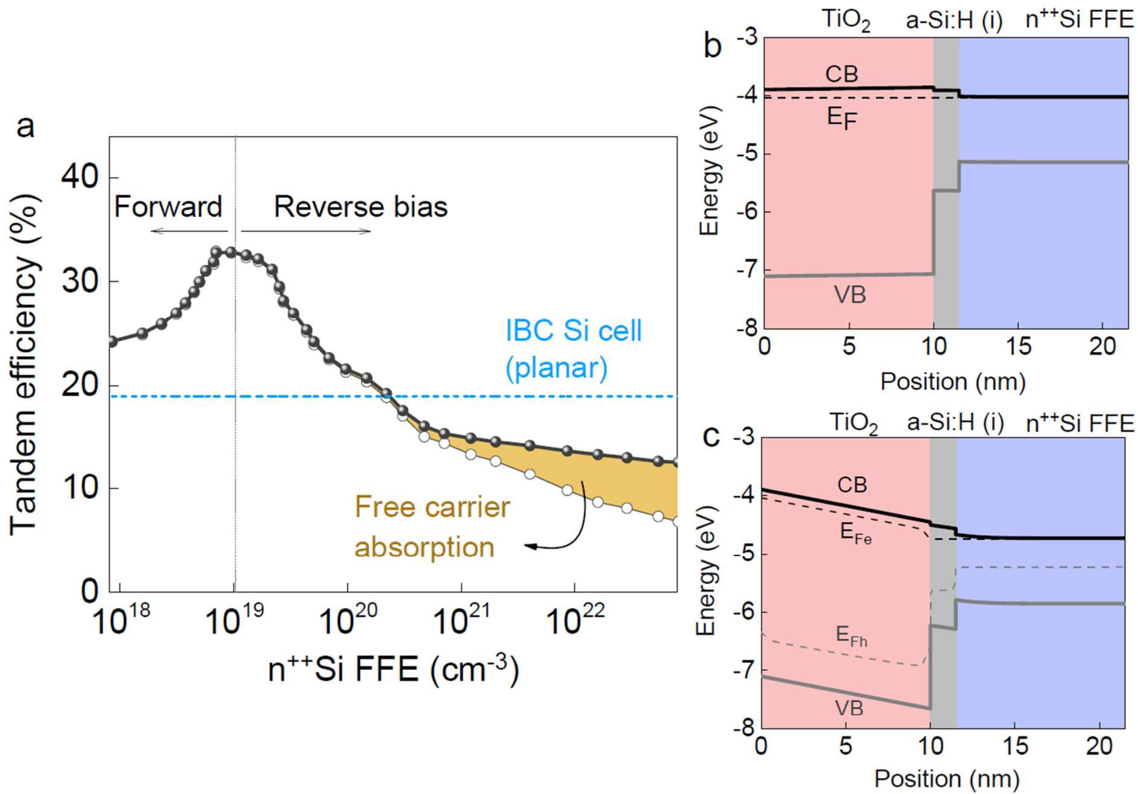

Figure S6. Tandem efficiency dependence on the tunnelling layer. (a) Tandem efficiency (perovskite L_D = 10 μm) versus doping concentration of n^{++}Si front floating emitter. The doping concentration determines the direction of minority carrier flow (in this case electron); forward or reverse bias. The tandem efficiencies were calculated with (open circles) and without (filled circles) the free carrier absorption effect of n^{++}Si FFE which is more significant at higher concentrations. It shows two regimes of successful forward tunnelling from perovskite-Si cells, and reverse tunnelling from n^{++}Si FFE to the perovskite cells. Simulated band diagram across the tunnelling layer at **(b)** thermal equilibrium, **(c)** forward bias condition.

We used the Ebers-Moll model[21,22] to describe how this tunnel junction works (e.g. using SPICE circuit simulation). In our simulation, we identify four criteria to ensure a successful electron tunnelling from perovskite to the silicon cell: (1) forward bias injection for both perovskite and silicon cells, (2) Fermi level alignment across the depletion region, (3) thickness (doping profile depth) of the n^{++}Si FFE, (4) doping concentration of the n^{++}Si FFE.

We simulate two main junctions involved between perovskite and silicon layer, both of which should be forward biased and saturated in the n^{++}Si FFE for successful tunnelling process (100% injection efficiency). Both junctions are $CH_3NH_3PbI_3/TiO_2$/a-Si:H (i)/n^{++}Si FFE (for the perovskite cell), and p-Si base/n^{++}Si FFE (for the Si cell). Any reverse injection occurring within the depletion region could potentially drop the injection efficiency.

We need to prevent this reverse charge injection (electron back flow) across the depletion region n^{++}Si FFE/a-Si:H(i)/TiO_2/perovskite interfaces. The main requirement is to maintain a rectification of charge injection by Fermi level alignment through the depletion region. In our simulations, this is clearly visible from a large valence band offset within the depletion region. As a result the tunnel layer will block any hole transport (majority carrier) from the p-Si base to the perovskite cell, hence the n^{++}Si FFE would selectively receive the generated electrons both from perovskite and Si cells. The carriers would then be injected into the p-Si base to be collected at the n^{++}Si rear emitter contact.

This condition alone does not prevent the possibility of reverse charge injection. This happens when there is a "cut-off" decay between n^{++}Si FFE and p-Si base, and/or very high doping concentration of n^{++}Si FFE relative to n^{++}Si rear emitter. In other words, a proper thickness of the n^{++}Si FFE with a proper doping concentration relative to the fixed p-Si base doping concentration is required. To maintain 100% injection, we use a 10 – 44 nm n^{++}Si FFE thickness, where the thickness less than 10 nm would give undesired excess carriers to be stored the n^{++}Si FFE instead of fully injected toward p-Si base. Any stored charge can be translated further as a reverse charge injection (theoretical details are well explained by C.Hu[22], and S. Datta[19].

Once we optimized the n++Si FFE decay width (thickness), we need to ensure that the doping concentration of n^{++}Si FFE is much higher than the p-Si base, but less than the n++Si rear emitter contact. Shortly, this implies a lower potential difference in the n^{++}Si FFE/p-Si base interface than in the n^{++}Si rear emitter/p-Si base interface, and as a result the minority carrier (electron) generated on the p-Si base (on top of the n^{++}Si rear emitter) will tend to diffuse toward n^{++}Si FFE rather than being collected on the n^{++}Si rear emitter contact.

Conversely, electron charge injection in the depletion region between n^{++}Si FFE to the p-Si base interface is necessary for transporting the electrons (minority carriers) generated in region above the p^{++}Si BSF contact, through n^{++}Si FFE, and to the n^{++}Si rear emitter and contact for collection. This allows one to make the n^{++} and p^{++} back contact regions equally sized and spaced as originally proposed in the (Mercury cell[20]) IBC-Si used in our simulations. In order to achieve this condition alone, we set the resistivity of the p-Si base to be ~13.5 to 15 times higher than that of the n^{++}Si FFE. In other words, the doping concentration of n^{++}Si FFE should be much higher than the p-Si base for a successful "re-pumping" injection, but lower than the n^{++}Si rear emitter to prevent a reverse charge injection.

In addition to the minimum required decay width for electron transition time from n^{++}Si FFE to the p-Si base, the doping concentration of n^{++}Si FFE also contributes to a free-carrier (parasitic) absorption that reduces the tandem efficiency. We computed the influence of a range of doping concentrations of n^{++}Si FFE on this effect (**Figure S6**).

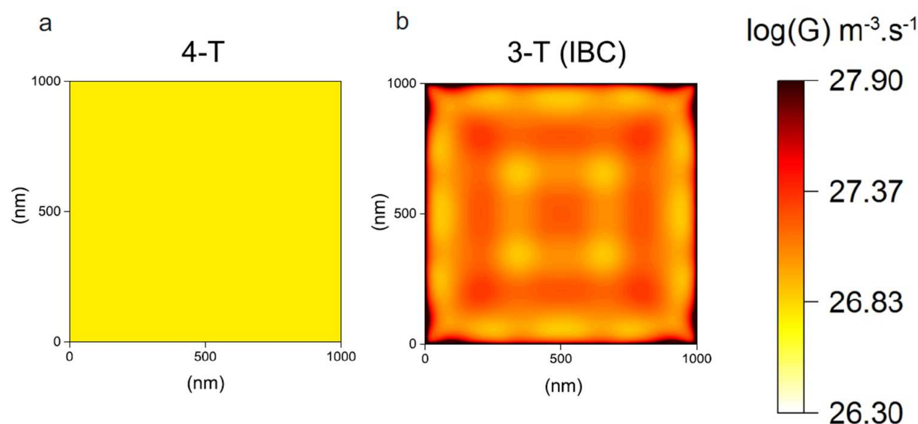

Figure S7. Charge generation rate near the perovskite bandgap (700-800 nm). (a) 4-T, and **(b)** 3-T (IBC), both of which are at their maximum performances (with perovskite thickness of 950 nm, and 550 nm (1 μm pitch) for 4-T and 3-T (IBC), respectively). The generation rate values are averaged over the perovskite thickness showing uniform generation on the 4-T, whereas a quadrupole generation toward the grid corners emerged on the 3-T (IBC). This is associated with the origin of the increased EQE in the 3-T (IBC) near the perovskite bandgap (**Fig. 4a**; main text).

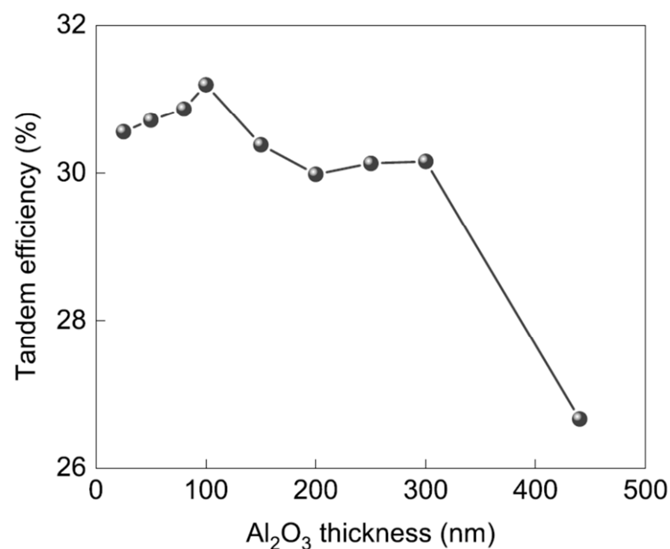

Figure S8. Positioning dependence of the nanogrid contact on 3-T (IBC) tandem efficiency (by varying insulator thickness). The simulation is performed using the optimized condition (550 nm perovskite thickness with 1 μm pitch). The tandem efficiency reaches maxima at 100 nm thick Al_2O_3 which further used on all of our simulations.

Table S2. PV parameters for the simulated textured cells.

Device		PV parameter			
		V_{oc} (V)	J_{sc} (mA/cm^2)	FF	PCE (%)
Perovskite	3T	1.23	23.86	0.84	24.77
	4T	1.19	22.53	0.86	23.17
Silicon	3T	0.67	19	0.83	10.5
	4T	0.66	17.6	0.83	9.67
Tandem	3T				35.27
	4T				32.84

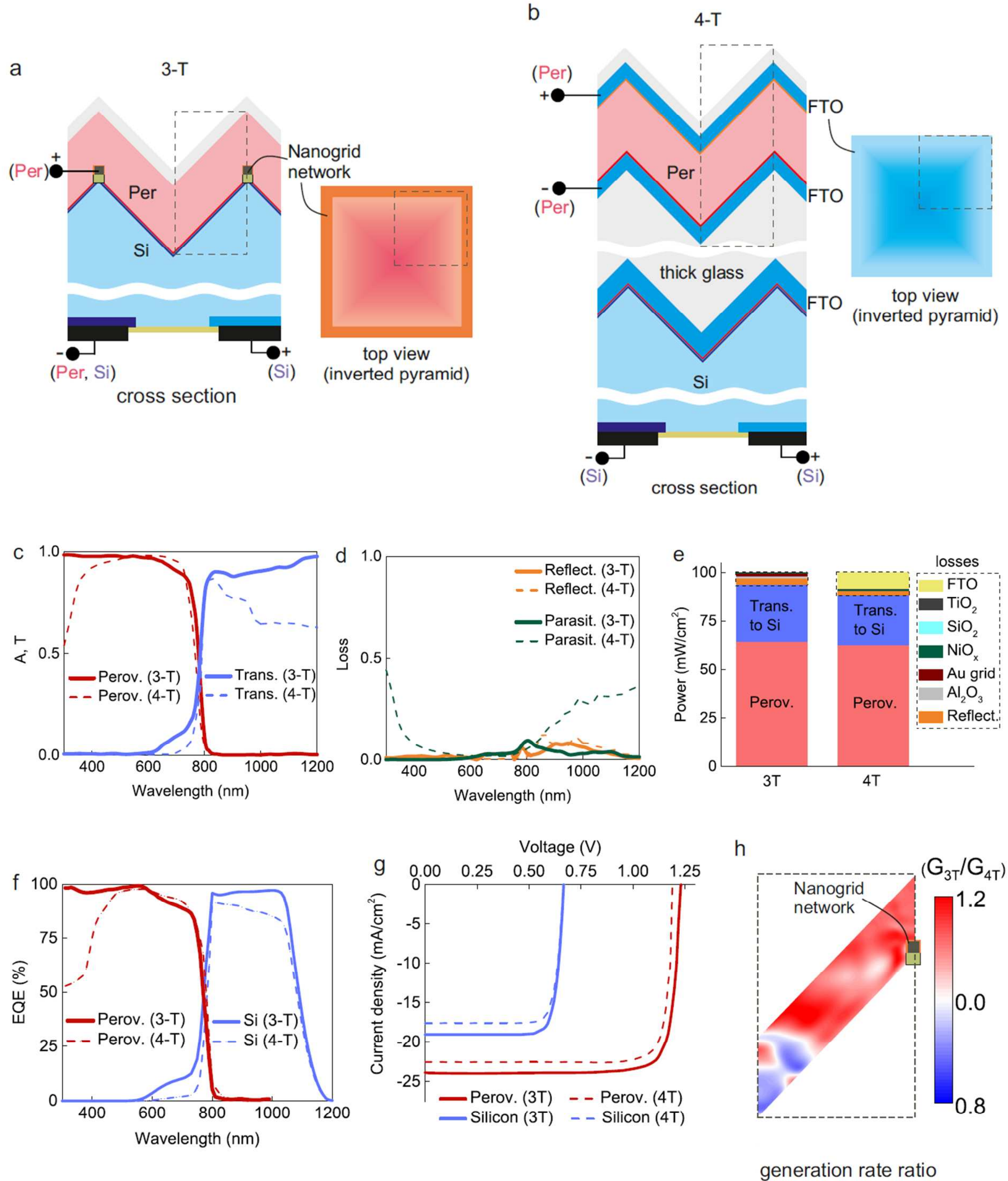

Figure S9. Textured cell simulations: perovskite-silicon tandem with 3-T (with nanoscale back contact perovskite) and 4-T configurations. **(a)** Schematic of the textured 3-T tandem with nanoscale back contact perovskite. **(b)** Schematic of the textured 4-T tandem. The dashed-green boxes represent the unit cell of our 3D coupled optical-electrical simulations. Note that both configurations use an optimized IBC-Si cell (25.03% efficiency with pitch size of 1.6 micron or equivalent to characteristic angle of 54.7°) and the same perovskite

thicknesses (550 nm) for an equivalent comparison. **(c)** Absorption spectra of the perovskite, and transmission through to the silicon cell. **(d)** Total loss spectra due to reflection and parasitic absorption. **(e)** Total optical power contribution of each layer integrated over AM 1.5 standard spectrum. **(f)** I-V curve independently extracted from the perovskite and silicon cells (corresponding values are tabulated in **Table S2**). **(g)** EQE spectra independently extracted from the perovskite and silicon cells. **(h)** cross-section view of generation rate ratio between 3T and 4T (G_{3T}/G_{4T}) within a unit cell of the textured perovskite, showing the generation rate is enhanced toward the nanogrid contact. This generation rate is integrated over the AM 1.5 standard spectrum. The electrical simulation was done with a 10 micron diffusion length perovskite, with all coupled optical-electrical simulations carried out in 3D.

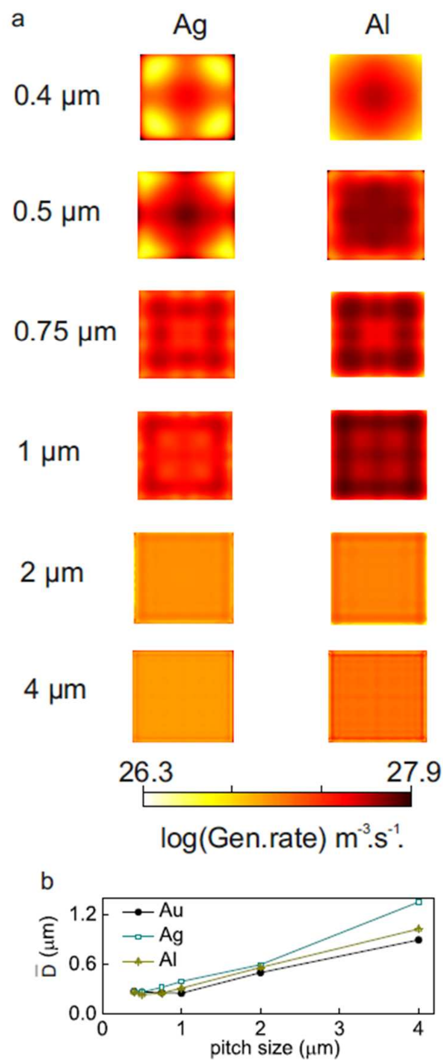

Figure S10. Photonic cavity effect using different grid metals. **(a)** Top view of charge generation rate in 3-T (IBC) showing charge concentration toward the contact (edges of the squares) as the pitch size (values indicated on the most left) increases. Similar to Figure 5c-d, the generation rate profiles presented here are already integrated over the AM 1.5 solar spectrum, and averaged over the perovskite thickness inside the cavity. **(b)** Calculated effective collection distance ($\overline{D}$) as a function of pitch size. There is a slight shift of the minimum $\overline{D}$ using different metal, however the general trend is the same regardless of metal used, indicating the effect is due more to the creation of a photonic cavity than plasmonic enhancement.

Supplementary references

1 Löper, P.; Stuckelberger, M. ; Niesen, B.; Werner, J.; Filipič, M.; Moon, S-J.; Yum, J-H.; Topič, M.; Wolf, S. D.; Ballif, C.; *J. Phys. Chem. Lett.* **2015**, *6*, 66–71.

2 De Wolf, S.; Holovsky, J.; Moon, S-J.; Löper, P.; Niesen, B.; Ledinsk, M.; Haug, F-J.; Yum, J-H.; Ballif, C. *J. Phys. Chem. Lett.* **2014***, 5,* 1035–1039.

3 Green, M. A. *Sol.Energy Mat. & Solar Cells* **2008**, *92*, 1305–1310.

4 Ball, J.M.; Stranks S.D.; Hörantner, M.T.; Hüttner, S.; Zhang, W.; Crossland, E.J.W.; Ramirez, I.; Riede, M.; Johnston, M.B.; Friend, R.H.; Snaith, H.J. *Energy Environ. Sci.* **2015**, *8*, 602–609.

5 Pierce, D. T.; Spicer, W. E. *Phys. Rev. B*. **1972**, *5*, 3017–3029.

6 Baker-Finch, S.; McIntosh, K. R. *Prog. in Photovolt.: Research and Applications* **2011**, *19*, 406–416.

7 Palik, E. Vol. 1 2 (Academic Press, Orlando, 1985).

8 Johnson, P. B.; Christy, R. W. *Phys Rev B.* **1972**, *6*, 4370–4379.

9 *FDTD Solutions*, http://www.lumerical.com (access date 12 March 2017).

10 Baker-Finch, S. C.; McIntosh, K. R. *35th IEEE Photovoltaic Specialists Conference*, Honolulu, **2010**, 2184–2187.

11 Green, M. A. Sol.-State Elec. **1981**, *24*, 788–789.

12 Baker-Finch, S-C.; McIntosh, K.R.; Yan, D.; Fong, K.C.; Kho, T.C. *J. App. Phys.* **2014**, *116*, 1–12.

13 Stranks, S. D.; Eperon, G. E.; Grancini, G.; Menelaou, C.; Alcocer, M. J. P.; Leijtens, T.; Herz, L. M.; Petrozza, A.; Snaith, H. J. *Science* **2013**, *342*, 341–344.

14 Almansouri, I.; Green, M. A.; Ho-Baillie, A. *Journal of Materials Research* **2016**, *31*, 2197–2203.

15 Varache, R.; Leendertz, C.; Gueunier-Farret, M. E.; Haschke, J.; Muñoz, D.; Korte, L. S*ol. Energy Mat. & Solar Cells*, **2015**, *141*, 14–23.

16 *DEVICE CT Solutions*, http://www.lumerical.com (access date 12 March 2017).

17 Fell, A.; Fong, K. C.; McIntosh, K. R.; Franklin, E.; Blakers, A. W. *IEEE Journal of Photovoltaics* **2014**, *4*, 1040–1045.

18 Correa-Baena, J-P.; Anaya, M.; Lozano, G.; Tress, W.; Domanski, K.; Saliba, M.; Matsui, T.; Jacobsson, T. J.; Calvo, M. E.; Abate, A.; Grätzel, M.; Míguez, H.; Hagfeldt, A. *Advanced Materials*, **2016**, *28*, 5031–5037.

19 Datta, S. *Electronic transport in mesoscopic systems*. Cambridge University Press, New York, **1995**, 285–308.

20 Cesar, I.; Guillevin, N.; Burgers, A. R.; Mewe, A. A.; Koppes, M.; Anker, J.; Geerligs, L. J.; Weeber, A. W. *Energy Procedia* **2014**, *55*, 633–642.

21 Sze, S. M. *Physics of Semiconductor Devices*. John Wiley & Sons, Canada, **1981**, 243–290.

22 Hu, C. C. *Modern Semiconductor Devices for Integrated Circuits*. 351 Prentice Hall, New Jersey, **2010**, 291–324.

23 Yaghjian, A. D. *IEEE Trans. Antennas. Propag*. **2007**, *55*, 1495 – 1505.